Published in "ACS Applied Nano Materials 2(7): 4462–4470, 2019"
which should be cited to refer to this work.

Phase Transformation of Superparamagnetic Iron Oxide Nanoparticles via Thermal Annealing: Implications for Hyperthermia Applications

Federica Crippa,[†] Laura Rodriguez-Lorenzo,[†,‡] Xiao Hua,[†] Bart Goris,[§] Sara Bals,[§] José S. Garitaonandia,[∥] Sandor Balog,[†] David Burnand,[†,⊥] Ann M. Hirt,[#] Laetitia Haeni,[†] Marco Lattuada,[⊥] Barbara Rothen-Rutishauser,[†] and Alke Petri-Fink*[,†,⊥]

[†]Adolphe Merkle Institute, University of Fribourg, Fribourg, Switzerland
[‡]Water4Environment Unit, International Iberian Nanotechnology Laboratory, Braga, Portugal
[§]Electron Microscopy for Materials Research, University of Antwerp, Antwerp, Belgium
[∥]Zientzia eta Teknologia Fakultatea. Euskal Herriko Unibertsitatea, Bilbao, Spain
[⊥]Chemistry Department, University of Fribourg, Fribourg, Switzerland
[#]Institute for Geophysics, ETH Zurich, Zurich, Switzerland

S *Supporting Information*

ABSTRACT: Magnetic hyperthermia has the potential to play an important role in cancer therapy and its efficacy relies on the nanomaterials selected. Superparamagnetic iron oxide nanoparticles (SPIONs) are excellent candidates due to the ability of producing enough heat to kill tumor cells by thermal ablation. However, their heating properties depend strongly on crystalline structure and size, which may not be controlled and tuned during the synthetic process; therefore, a postprocessing is needed. We show how thermal annealing can be simultaneously coupled with ligand exchange to stabilize the SPIONs in polar solvents and to modify their crystal structure, which improves hyperthermia behavior. Using high-resolution transmission electron microscopy, X-ray diffraction, Mössbauer spectroscopy, vibrating sample magnetometry, and lock-in thermography, we systematically investigate the impact of size and ligand exchange procedure on crystallinity, their magnetism, and heating ability. We describe a valid and simple approach to optimize SPIONs for hyperthermia by carefully controlling the size, colloidal stability, and crystallinity.

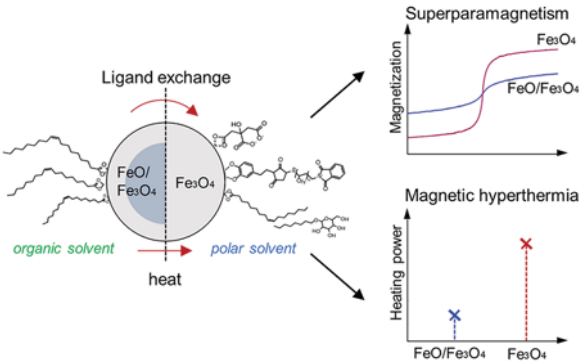

KEYWORDS: *magnetic nanoparticles, superparamagnetism, ligand exchange, thermal annealing, magnetic hyperthermia*

INTRODUCTION

Magnetic hyperthermia that employs nanomaterials has unique advantages, including spatiotemporally controlled treatment of the targeted disease in a noninvasive manner.[1−3] Superparamagnetic iron oxide nanoparticles (SPIONs) have been widely investigated for use in hyperthermia treatment of cancer due to their exceptional capability to generate thermal energy in alternating magnetic fields at the targeted area.[4,5] This ability to act as "heaters" is strongly correlated to a narrow particle size distribution, their superparamagnetic behavior, and crystal structure.[4,6,7] However, challenges associated with SPIONs relate to their intrinsic colloidal instability in physiological conditions and the impossibility to precisely tune their crystallinity by adapting the synthesis procedure.[8−14] Therefore, it is crucial to develop strategies to enhance the particles' colloidal stability and to adjust their crystallinity as desired.

In this study, we investigated systematically the use of ligand exchange processes to simultaneously transfer and to stabilize SPIONs in aqueous suspensions that are suitable for magnetic hyperthermia and to obtain monocrystalline particles of a defined crystalline phase, i.e., magnetite (Fe_3O_4) (Scheme 1). Following the thermal decomposition method, i.e., the most common method to obtain low-polydisperse SPIONs with well-defined size and shape,[15,16] we synthesized two different SPIONs batches that are characterized by different nominal sizes and observed how the SPIONs' crystalline structure varied with size. With this synthetic procedure, wüstite crystals as well as spherical, cubical, and octahedral particles containing a wüstite core (FeO) and a spinel shell have been reported in

Scheme 1. Synthesis and Functionalization of SPIONs[a]

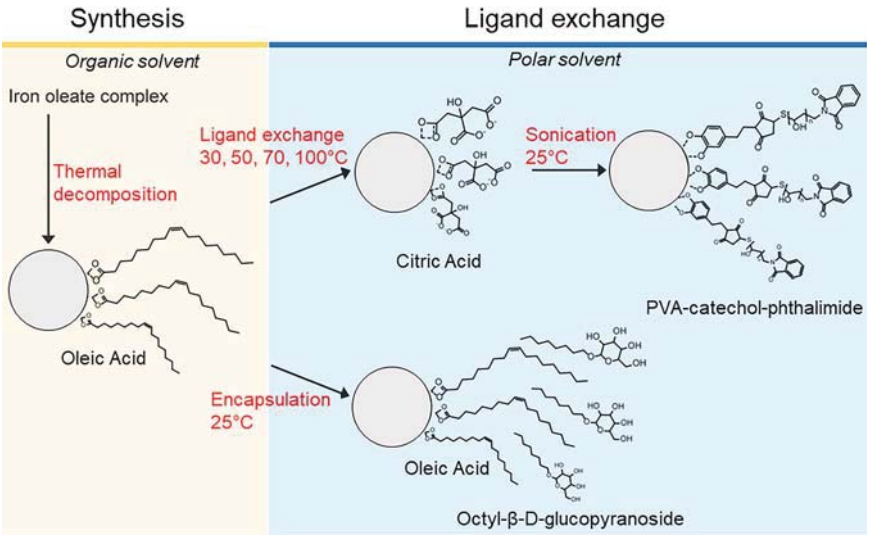

[a]Oleic acid-coated particles, obtained by thermal decomposition of a preformed iron oleate complex, were stable in organic solvents. SPIONs were then transferred to water by (1) exchanging the oleic acid with citric acid (at different reaction temperatures) or by (2) encapsulation in octyl-β-D-glucopyranoside. Citrate particles were further functionalized with PVA-catechol-phthalimide to ensure stability in biological media.

the literature as a direct outcome of their synthesis.[8−12,14,17] These crystals typically show poor superparamagnetic properties[18,19] and must be converted to pure spinel phases (either magnetite or maghemite) to be efficiently used as cancer eradicators.[20] Therefore, we also investigate how ligand exchange processes can be used to directly alter the crystal phase of SPIONs at the same time as transferring the particles to polar solvents to enhance their applicability in biomedical applications.[21−23] Finally, we correlated the crystalline phases with the magnetic properties, and we studied how these parameters influence the hyperthermia behavior.

EXPERIMENTAL SECTION

Materials. All chemicals were of analytical reagent grade unless further specified and were used without any purification. Iron(III) chloride hexahydrate (99%), oleic acid (technical grade, 90%), citric acid (99.5%), *N*,*N*-dimethylformamide (DMF, 99.8%), 1,2-dichlorobenzene (DCB, 99%), hydrochloric acid (HCl, 37%), nitric acid (HNO_3, 65%), and diethyl ether (99%) were supplied by Sigma-Aldrich. Sodium oleate (97%) and tri-*n*-octylamine (97%) were purchased from TCI. Absolute ethanol and acetone were purchased from VWR Chemicals. Octyl-β-D-glucopyranoside was purchased from Alexis Biochemicals. All aqueous solutions were prepared with deionized water obtained from a Milli-Q system (resistivity = 18.2 Ω, Millipore AG).

Particles Synthesis and Functionalization. *SPIONs Synthesis.* Iron oxide nanoparticles with average diameters of 10 and 20 nm (10-OA and 20-OA) were synthesized by thermal decomposition of the iron oleate complex according to a modified literature procedure.[15] Briefly, the iron oleate complex (15.9 g), prepared by reacting iron chloride ($FeCl_3 \cdot 6H_2O$, 8.6 g) with sodium oleate (29.8 g), was heated to 320 °C in the presence of oleic acid (2.5 g) in tri-*n*-octylamine (115.2 mL). The solution was heated as follows: 25 to 100 °C, heating rate = 10 °C/min; 100 to 196 °C, heating rate = 4.5 °C/min; 196 to 320 °C, heating rate = 3 °C/min. The final temperature was kept for 30 min (10 nm particles) or 1 h (20 nm particles). Then the solution was quickly cooled to 25 °C in 10 min (10 nm particles) or 30 min (20 nm particles). Afterward, the nanoparticles were separated by three sequential centrifugations as follows: 3 min at 30000*g* in a solution of hexane and ethanol (ratio 1:5). The resulting oleic acid-coated nanoparticles were redispersed in different organic solvents (hexane, chloroform, or toluene) and stored at 4 °C. Particles stored in hexane were stabilized by adding an excess of oleic acid (0.12 mg of oleic acid/mg of Fe).

Citric Acid Coating. A ligand exchange procedure was performed to exchange oleic acid on the SPIONs surface with citric acid yielding nanoparticles stable in polar solvents.[24] For this, SPIONs were dispersed in a solvents' mixture of DCB and DMF (ratio 1:1). Citric acid was then added (0.8 mg of citric acid/mg of Fe), and suspensions were stirred for 48 or 24 h at different temperatures: 30 °C (48 h) and 50, 70, and 100 °C (24 h). Following this, the nanoparticles were precipitated in 200 mL of diethyl ether and recovered with a magnet (nickel-plated NdFeB, Supermagnete). The resulting citric acid-coated SPIONs were washed in acetone and finally redispersed in Milli-Q water.

PVA-Catechol Coating. PVA-catechol (M_w = 5 kDa) was synthesized by following a previously described procedure[25] and coupled to the citric acid-coated particles (7 mg of PVA-catechol/mg of Fe) leading to an initial grafting density of 10 molecules/nm^2. The suspensions containing the particles and the polymer were sonicated overnight.

Surfactant Coating. 9 mg of 20 nm oleic acid SPIONs were transferred from hexane to 1 mL of chloroform. 38 mg of octyl-β-D-glucopyranoside (M_w = 292.37) were dissolved in 1 mL of Milli-Q water, and the SPIONs suspension was slowly added to the surfactant solution. The final suspension was sonicated for 40 min to evaporate the chloroform, and the particles were finally resuspended in 2 mL of Milli-Q water.

Particles Characterization: TEM, DLS, ζ-Potential, and Iron Quantification. The size and morphology of citric acid SPIONs were investigated by transmission electron microscopy (TEM). Samples were prepared by drying the nanoparticle suspensions on copper carbon-coated mesh grids. Micrographs were acquired with a Tecnai Spirit transmission electron microscope (FEI) operating at 120 kV and equipped with a Veleta CCD camera (Olympus). The core diameters of the nanoparticles were estimated with automatized size distribution analysis software (ImageJ, National Institutes of Health).

Complementary investigation of SPIONs' size and colloidal stability was performed with a dynamic light scattering (DLS) setup (3D LS spectrometer, LS Instruments AG). The suspension was diluted to a low concentration (0.05 mg/mL Fe) to avoid multiple light scattering. Data were collected at 25 °C with a scattering angle of 90° and were analyzed with a customized script in Mathematica

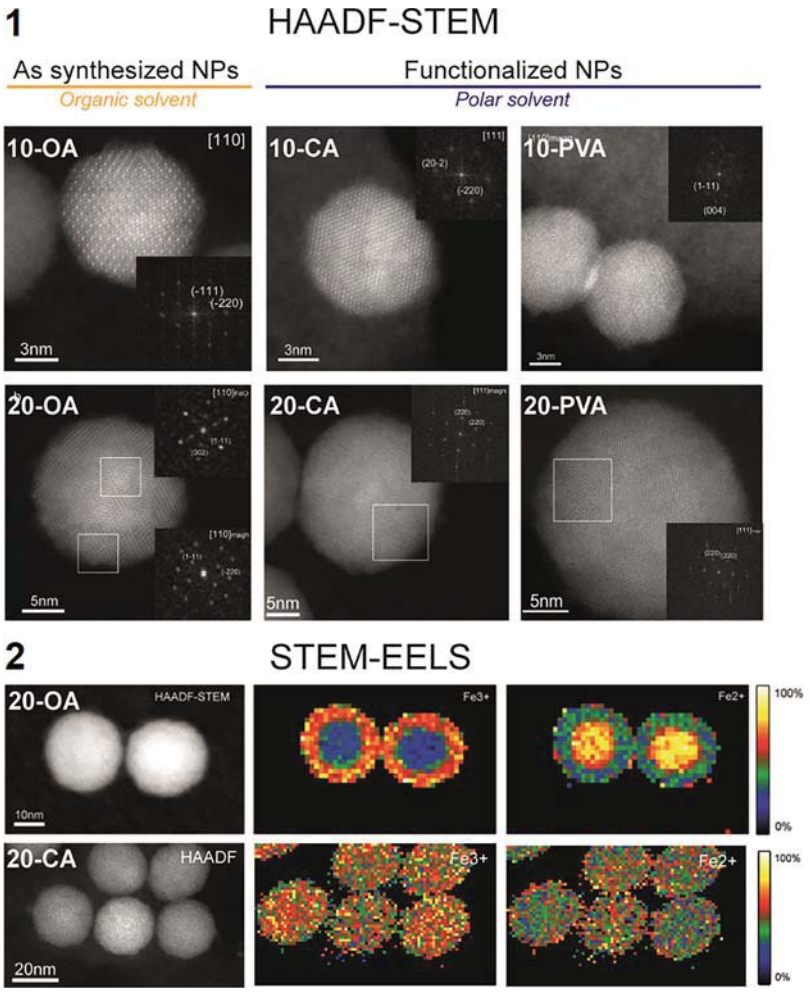

Figure 1. (1) HAADF-STEM and (2) STEM-EELS of 10 and 20 nm SPIONs before and after ligand exchange. High-resolution HAADF-STEM images of 10-OA, 10-CA, and 10-PVA reveal the presence of a single magnetite (Fe_3O_4) crystal. The crystalline structure of 20-OA was investigated with high-resolution HAADF-STEM, STEM-EELS: HAADF-STEM analysis indicated the presence of a mixture of wüstite and spinel-like phases (magnetite or maghemite (γ-Fe_2O_3)). 20-CA and 20-PVA, functionalized at 100 °C, show the presence of a single crystal of magnetite (HAADF-STEM, STEM-EELS).

(Version 10.1, Wolfram Research Inc.) developed to selectively remove spikes arising from small clusters and dust.[26]

The efficiency of the coating for citrate- and PVA-catechol-coated particles was checked with ζ-potential measurements performed with a commercial device (90Plus zeta-potential analyzer, Brookhaven Instruments Corp).

The iron concentration of the SPIONs was quantified by using inductively coupled plasma optical emission spectroscopy (ICP-EOS, PerkinElmer Optima 700 DV). Samples were prepared by a two-step microwave-assisted digestion (Multiwave PRO, Microwave Reaction System, Anton Paar): 10 μL of each suspension was predissolved in a mixture of HNO_3, H_2O_2, and Milli-Q water and subsequently redigested in HCl. Each experiment was repeated in triplicate three times.

Crystalline Structure Analysis: High-Resolution HAADF-STEM, EELS, and XRD. All samples were investigated by using an aberration-corrected Titan microscope operated at 120 kV. To identify the crystalline phase of the nanoparticles, both high angle annular dark field (HAADF) scanning transmission electron microscopy (STEM) imaging and electron energy loss spectroscopy (EELS) experiments were performed.

X-ray diffraction (XRD) patterns were collected on an Ultima IV X-ray diffractometer (Rigaku, Japan, Cu Kα, 2θ measuring range: 20°−80°). To identify phase composition and weight fraction, the data were analyzed by using Match3 X-ray powder diffraction software (Crystal Impact GbR) followed by Rietveld refinement.

Magnetic Measurements: VSM and Hyperthermia Characterization. The magnetic properties of the SPIONs were investigated with a vibrating sample magnetometer (VSM, Model 3900, Princeton Measurements Corp.). The samples were dried on hydrophobic cotton pellets and fixed on the sample holder with Si grease. Magnetization was measured at room and low temperature as a function of the magnetic field. The hysteresis loops at room temperature were recorded by using a measurement averaging time of 300 ms and a constant field increment. Low-temperature measurements were made with the same instrument with a PCM cryostat and using an averaging time of 500 ms to improve the signal-to-noise ratio. Data were collected, and the magnetic moment was normalized by the iron mass to obtain magnetization.

The hyperthermia properties of all nanoparticles were investigated with a new technique based on lock-in thermography (LIT) recently described.[27] All magnetic field experiments were performed on a commercial alternating magnetic field generator (Magnetherm V1.5, Nanotherics Ltd.) operating at 523.4 kHz and 14.7 kA/m. LIT recordings and analyses were performed as previously described[28] at a modulation frequency of 1 Hz over 200 cycles.

Mössbauer Spectroscopy. Mössbauer spectroscopy measurements were performed in transmission geometry using a conventional constant-acceleration spectrometer with ^{57}Co−Rh source. Spectra were collected at different temperatures under high vacuum (10−6 Torr) in a commercial Janis He closed cycle cryostat. The isomer shift values were taken with respect to an α-Fe calibration foil measured at

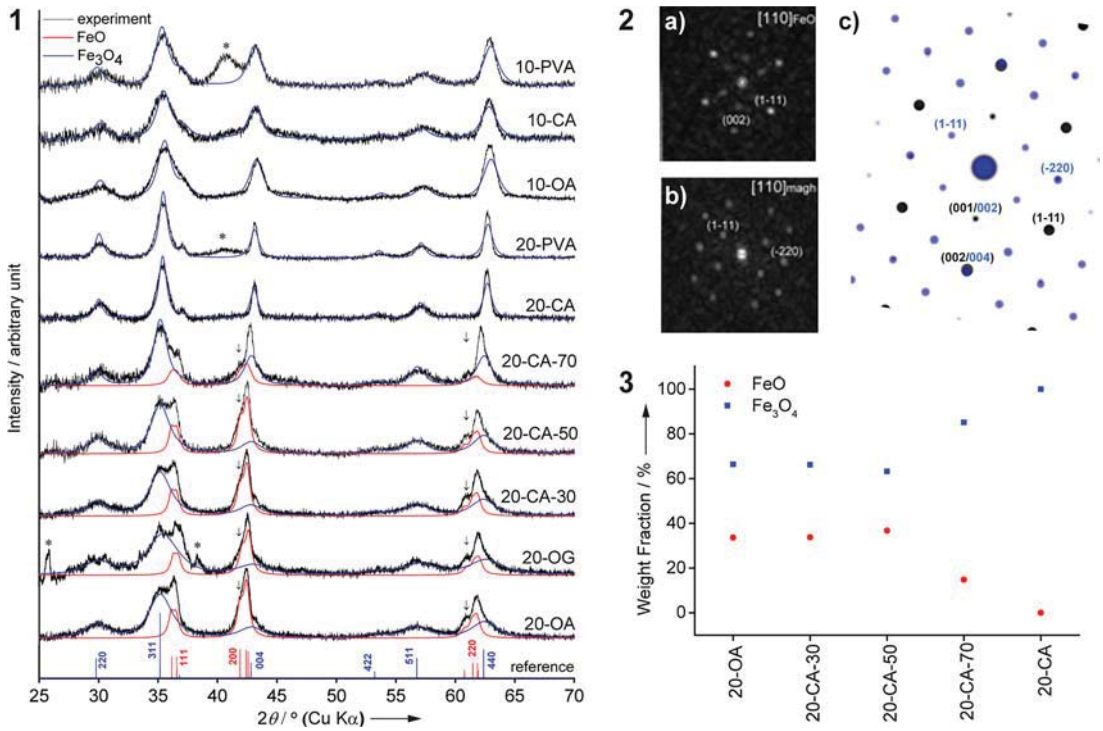

Figure 2. XRD characterization of 10 and 20 nm SPIONs before and after ligand exchange. (1) XRD patterns of the SPIONs in comparison with the contributions of Fe_3O_4 ($Fd\bar{3}m$) (blue) and FeO ($C2/m$) (red) from Rietveld refinement of each data. References are shown below with main reflections labeled. Asterisk marks impurity, and arrows denote additional reflections from the structure distortion. (2) ED of the 20-OA sample from (a) core and (b) shell. (c) ED simulation (viewed along the [110] zone axis of FeO), using the Fe_3O_4 ($Fd\bar{3}m$) (blue) and FeO ($C2/m$) (black) structures obtained from the XRD refinement of 20-OA data. Reflections from different phases are labeled by using the same color code. (3) Weight fractions of the FeO and Fe_3O_4 phases from the refinements.

room temperature. To avoid potential changes in the oxidation state of the nanoparticles during the measurements, spectra were collected as received with the SPIONs suspended in appropriated solvent (CA coating in water and OA coating in hexane). NORMOS program developed by Brand et al.[29] was used for peak fitting of the experimental spectra.

RESULTS AND DISCUSSION

The as-synthesized oleic acid (OA)-coated SPIONs display a spherical shape and high monodispersity with an average diameter of 9.5 ± 0.4 and 20.2 ± 1.6 nm, respectively. They are colloidally stable in organic solvents (Supporting Information, Figure S1 and Table S.1). These two particle batches will be termed 10-OA and 20-OA in the following text. Figures 1 and 2 show high-resolution transmission electron microscopy (HR-TEM) images and X-ray diffraction (XRD) analyses of both batches of OA-coated SPIONs, respectively, where two distinct crystalline phases can be identified within the particles. While 10-OA consists of a single magnetite domain, 20-OA shows a more complex core/shell structure.

Throughout the high-angle annular dark-field scanning TEM (HAADF-STEM) image and oxidation state maps, which were obtained from electron energy loss spectroscopy (STEM-EELS) (Figures 1.1 and 1.2), a core−shell structure is identified, which is composed of a magnetite shell surrounding a wüstite core. XRD analysis and Mössbauer spectroscopy confirm the observed compositions (Figure 2 and Figure S2, respectively).

In particular, XRD patterns of 10-OA support a magnetite phase, while a more complex structure is found for 20-OA (Figure 2, more details on estimated crystalline size in Table S.2). To achieve a more reliable phase and structure determination, Rietveld refinement was attempted using the Fe_3O_4 (space group $Fd\bar{3}m$) and FeO ($Fm\bar{3}m$) structures based on the electron diffraction (ED) data. However, the combination of the two cubic iron oxides could not be resolved from the shoulder peaks at 42° and 61° 2θ (marked by arrows in Figure 2.1), suggesting either a deviation of the actual particle from the cubic structure or the potential presence of a third phase. The ED from the shell (Figure 2.2.b) is consistent with a cubic Fe_3O_4 structure. However, the ED of the core region (Figure 2.2.a), which contains scattering from both the core and shell of the particle, shows an additional reflection, which could be assigned to either (001) for FeO or (002) for Fe_3O_4. These reflections are, however, forbidden in the cubic symmetry, suggesting a possible deviation from this symmetry. Because the ED from the shell of the particle is compatible with a cubic Fe_3O_4, we thus investigated further a distortion of the cubic FeO in the core. This structural deviation, if it occurs, resides most likely in the core−shell interface associated with an inhomogeneous distribution of Fe^{2+} and Fe^{3+}, thus reflecting a structure transition from FeO to Fe_3O_4. Therefore, we performed a series of refinements incorporating a monoclinically distorted FeO structure ($C2/m$)[30] to represent an average structure between the FeO core and Fe_xO_y interface. Given the small length scale of this structural feature whose complexity lies on the atomic level, the refinement results were qualitatively satisfactory as it was challenging to disentangle this interface from the whole particle for a precise structural analysis using the conventional diffraction method.

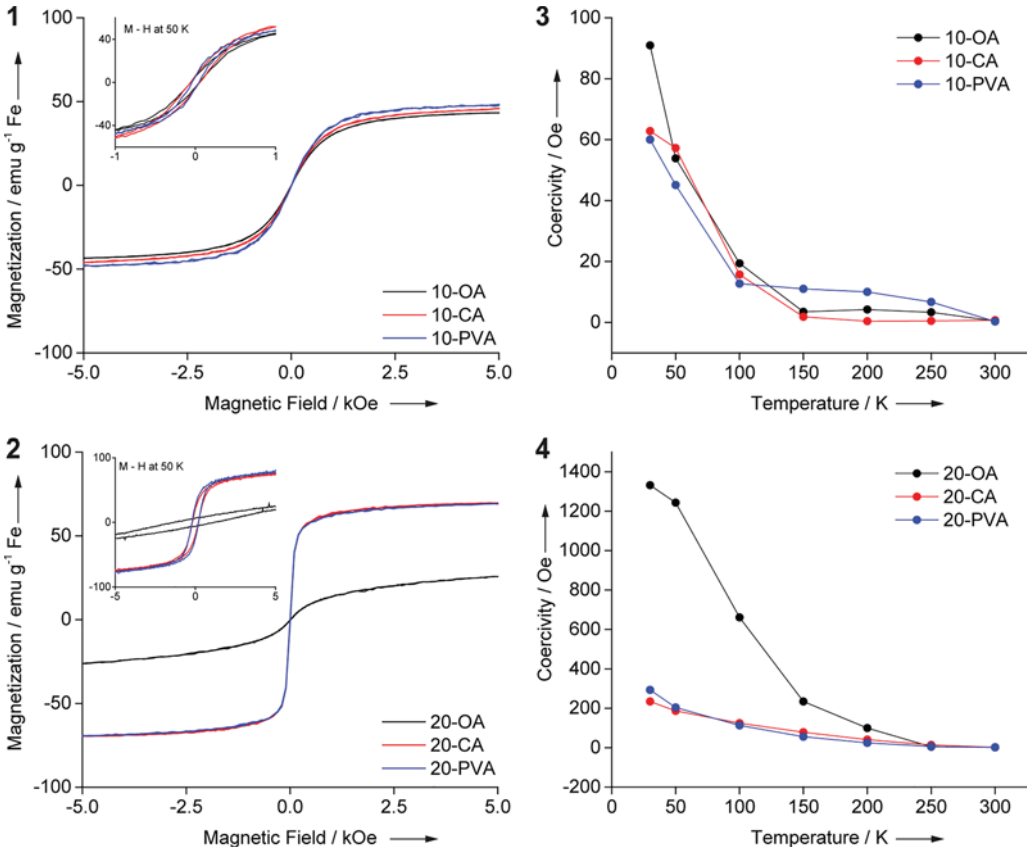

Figure 3. Magnetic behavior of 10 and 20 nm SPIONs functionalized with different coatings. Magnetic hysteresis curves at 300 K for 10 nm (1) and 20 nm particles, (2) coated with oleic acid (OA), citric acid (CA), and PVA. Coercivity values, (3) and (4), as determined from the magnetic hysteresis curves performed at different temperatures (Figure S8). Small nanoparticles (10-OA, 10-CA, and 10-PVA) composed of a single core of magnetite are superparamagnetic independent of the coating. The 20 nm SPIONs display different magnetization behaviors in relation to their crystalline structure. 20-OA particles consist of a mixture of superparamagnetic and a phase with high-field susceptibility at 300 K. N.B.: at 50 K (inset) the 20-OA loop opens as the particles undergo blocking, which leads to an increase in coercivity (4); this low-temperature phase is ascribed to wüstite and its interface with the magnetite shell. Upon the oxidation of FeO to Fe_3O_4, 20-CA and 20-PVA show superparamagnetic behavior that blocks at low temperature (4).

The contribution of the Fe_3O_4 shell and FeO core that is calculated from these refinements is shown in Figure 2.1, with their respective weight fractions shown in Figure 2.3. An ED simulation (Figure 2.2.c) of the core−shell structure using the (cubic) Fe_3O_4 and (distorted) FeO structure refined from the 20-OA data shows a good agreement with the experimental observation (Figure 2.2.a). These results indicate that the oxidation of FeO in the 20-CA series leads to the formation of Fe_3O_4 which most likely commences at the surface of the particle when the annealing temperature reaches 50 °C. The FeO/Fe_3O_4 phase boundary, represented by an interface with a distorted cubic Fe_xO_y structure, progressively migrates from the surface to the core upon increasing the annealing temperature until the FeO is fully oxidized to Fe_3O_4.

Mössbauer spectra of both OA SPIONs samples supported the crystalline structures described above using XRD and HR-TEM data (Figure S2). While Mössbauer spectra of 10-OA and their hyperfine parameters fit a magnetite phase,[31] the analysis of 20-OA hyperfine parameters illustrates the contribution of Fe^{3+} A sites and the $Fe^{2+/3+}$ B sites of the inverse spinel structure of magnetite, and Fe^{2+} with possibly some Fe^{3+} of a wüstite phase[9,10,32,33] (more details in Figures S2.1 and S2.2 and Tables S.3 and S.4).

In general, the presence of the FeO phase is related to reduction phenomena occurring during the thermal decomposition of iron oleate where the production of CO and H_2 reductive gases reduces Fe^{3+} to Fe^{2+}, resulting in the generation of FeO crystals. As wüstite is a nonstoichiometric thermodynamically unstable compound,[34] Fe^{2+} ions tend to be quickly oxidized to Fe^{3+}, resulting in a spinel-type oxide more stable thermodynamically.[8] In the case of 10-OA, the FeO crystals could be oxidized to magnetite during the synthesis process. For particles larger than 14 nm a complete oxidation does not occur, resulting in the formation of FeO/spinel-type oxide structures as observed for the 20-OA sample.[8]

At this point, it is clear that the crystallinity is not fully tuned during synthetic process in the larger SPIONs, which are the best candidate for hyperthermia.[4] Therefore, we explored postprocessing procedures to modify not only their crystallinity but also the colloidal stability of the SPIONs. We transferred both (10-OA and 20-OA) particles to water using citric acid (CA) at 100 °C for ligand exchange.[24] CA-coated particles, 10-CA and 20-CA, were then further functionalized with catechol-end-terminated poly(vinyl alcohol) (^{1}H NMR spectra in Figure S3)[25] to improve their colloidal stability in biological media (10-PVA and 20-PVA). Upon functionalization, the samples were characterized by dynamic light scattering (DLS), ζ-potential measurements (Table S.1), and TEM (Figures S4 and S5). The functionalization processes did not alter the crystal lattice of the smaller particles (10-OA): high-resolution

HAADF-STEM imaging of 10-CA and 10-PVA (Figure 1.1) shows a spinel-type oxide structure oriented along a [111] zone axis for 10-CA and along a [110] zone axis for 10-PVA. The difference between magnetite and maghemite (which has similar crystal structure) was analyzed by STEM-EELS, and these experiments indicated the presence of approximately 66% Fe^{3+} and 33% Fe^{2+} corresponding to magnetite for both type of nanoparticles (Figure S6). The refinement of the XRD patterns of 10-CA and 10-PVA showed that all Bragg reflections could be indexed and matched Fe_3O_4 magnetite (Figure 2.1, crystalline size in Table S.2). Moreover, Mössbauer analysis on 10-CA confirmed the presence of a single iron oxide phase (i.e., magnetite) as observed for 10-OA (Figure S2.3 and Table S.5).

Because of the peculiar crystalline structure of 20-OA, these particles were functionalized not only with the procedure mentioned above but also with different methods to investigate the effects on the crystal oxidation. Therefore, the nanoparticles were functionalized with octyl-β-D-glucopyranoside (OG) and by ligand exchange with CA varying the reaction temperature (Scheme 1 and Table S.1). OG functionalization was chosen as it has been proven to be appropriate for SPIONs encapsulation in liposomes[35] while CA functionalization, a more robust ligand exchange, allowed us to vary the reaction temperature without altering the ligands. With this series of experiments, we could show that the reaction temperature during phase exchange is the crucial parameter steering the oxidation of the wüstite core toward magnetite, while ligand exchange promotes colloidal stability in polar solvents, which is a basic requirement for any (biological) application.[2,24] SPIONs functionalized at room temperature with OG (20-OG) and at 30 and 50 °C with CA (20-CA-30 and 20-CA-50) preserved their crystalline structure independently from the functionalization protocol and the coating as shown by XRD analysis (Figure 2.1 and Table S.2). At higher temperature, the evolution of the weight fractions from Fe_3O_4 and FeO (Figure 2.3) indicates that the elevated temperature leads to a phase transformation of FeO to Fe_3O_4. When particles were functionalized at 100 °C (20-CA) and coated with PVA (20-PVA), the core of FeO is fully oxidized to magnetite. Mössbauer analysis of 20-CA confirms the fully oxidation, fitting with a magnetite phase (Figure S2.4 and Table S.6).

High-resolution HAADF-STEM and STEM-EELS measurements corroborate the XRD data. Both measurements of 20-CA and 20-PVA indicate the absence of a core/shell structure; EELS results on 20-CA show a composition of 66% Fe^{3+} and 33% Fe^{2+} throughout the nanoparticles, corresponding to a magnetite crystal (Figure 1.2). We also investigated the role of CA in the oxidation process. Here, we annealed the 20-OA sample at 100 °C in the absence of CA by performing the same ligand exchange used for the 20-CA sample[24] but avoiding the addition of CA in the process. This resulted in destabilization of the particles, which quickly aggregated both in polar and in organic solvents, due to partial release of OA from their surface.[36] XRD analysis confirmed the oxidation of these particles (Figure S7); however, because of their intrinsic colloidal instability it was not possible to further characterize this sample and to perform, for example, magnetic hyperthermia measurements. Nevertheless, this experiment clarified the role of CA that solely promotes colloidal stability. On the other hand, the annealing process itself is responsible for the oxidation of FeO/Fe_3O_4 nanoparticles to Fe_3O_4 ones, as previously reported in the literature.[37]

The differences observed in the crystalline structures have a major impact on the magnetic properties of the analyzed nanoparticles. In the case of 10 nm SPIONs, the magnetic behavior, which has been investigated by vibrating sample magnetometry, is the same regardless of the coating (Figure 3.1). At 300 K, 10-OA, 10-CA, and 10-PVA show zero coercivity (Figure S8.1), indicating that the samples are superparamagnetic, while below 100 K the coercivity increases as particles undergo magnetic blocking (Figure 3.3). In all cases, the magnetic curves did not fully saturate and presented maximum magnetization that is lower than the saturation magnetization of magnetite (Ms = 92 emu/g).[34] These results can be due to the presence of a more oxidized contribution,[34] i.e., maghemite, or surface spin effects;[38] i.e., because of a high surface/volume ratio, a magnetic contribution from uncoupled spines from surface atoms is enhanced. Surface effects can dominate the overall magnetic behavior and strongly affect both saturation magnetization and ability to reach saturation for small oxide nanoparticles.[38−40] The 20 nm SPIONs display a different magnetization behavior related to their crystalline structure (Figure 3.2 and Figure S8 for 20-OA, 20-CA, and 20-PVA; Figure S9 for 20-CA-30, -50, and -70). While 20-CA and 20-PVA are superparamagnetic, the presence of the wüstite core of 20-OA, however, drastically decreases the particles' magnetization at 300 K. At lower temperatures 20-OA shows a pronounced increase in coercivity and is not close to saturation in the maximum field of 5 kOe (Figure 3.2, inset, and Figure 3.4). This behavior is related to wüstite as it undergoes magnetic ordering but may be also related to core−shell interactions arising at the interface of the two phases, as it has been previously shown in the literature.[8,10,37,41]

Nanoparticle size and crystalline structure are parameters that affect the particles' magnetization and have a major influence on the heating power of the SPIONs. We observe this by performing hyperthermia measures on our samples. To do so, we use a recently developed technique based on lock-in thermography,[27,28] in which the colloidal suspensions are excited with a modulated AMF and the heating signature is recorded with a synchronized IR camera and re-elaborated with a demodulation algorithm.[28] The resulting heating power of the nanoparticles is then expressed in terms of intrinsic loss of power (ILP, Figure 4).[42]

From the obtained data, we observed that small SPIONs (10-CA and 10-PVA) do not produce a detectable heat under the mentioned field conditions (frequency: 523.4 kHz; magnetic field amplitude: 14.7 kA/m). Indeed, considering the narrow size distribution of these particles and their shapes (Figure S1), the estimated crystalline size (Table S.2), and the low magnetization saturation (Figure 3.1), the thermal energy of 10-CA and 10-PVA is expected to be minimal according to the current understanding of magnetic hyperthermia phenomena based on the linear response theory (LRT).[4,43] When 10 nm magnetite nanoparticles are synthesized by means of the coprecipitation method, higher ILP values can be observed.[44] These results depend strongly on the fact that nanoparticles obtained by coprecipitation usually present high polydispersity (i.e., presence of nanoparticles much larger than the average 10 nm size) and high magnetization saturation due to low surface effects and fewer defects in crystallinity.

The 20 nm SPIONs with a wüstite/magnetite structure (20-OG, 20-CA-30, and 20-CA-50) has a weak signal. As expected, the sample functionalized at 70 °C (20-CA-70) generate more heat due to an increased presence of magnetite. In the presence

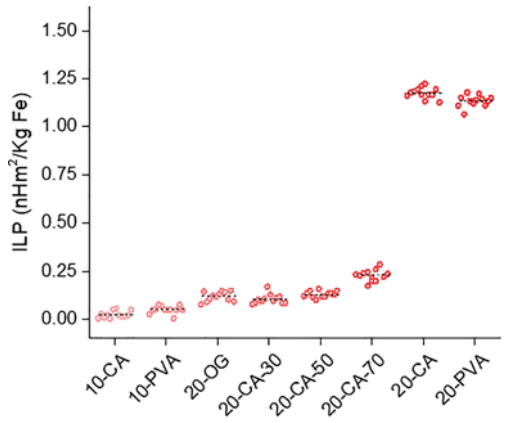

Figure 4. Particles' hyperthermia behavior obtained by lock-in thermography. SPIONs with different sizes and coatings were loaded in a customized low thermal emissivity sample holder and excited with an AMF (frequency: 523.4 kHz; magnetic field amplitude: 14.7 kA/m). Their thermal signature was recorded with the lock-in thermography system. The intrinsic loss power (ILP) values highlight the dependence of heating power on size and crystallinity.

of pure magnetite (20-CA), the ILP value was significantly enhanced more than 5 times and was not further changed upon functionalization with a catechol ligand (20-PVA).

When observing the results obtained for 10-CA, 10-PVA, 20-CA, and 20-PVA it is immediately evident that for the same experimental conditions, shape, crystal structure (i.e., magnetite), and colloidal stability, the diameter strongly influences the heating power. These results highlight the dramatic size effect and are in line with the current literature.[43,45] Indeed, when superparamagnetic nanoparticles are exposed to an alternating magnetic field, they dissipate heat through Néel and Brown relaxation phenomena as described before.[4] Both Néel and Brown relaxations depend on various parameters including particle diameter:[4] Néel relaxation shows an exponential dependency on the nanoparticle's magnetic volume, while Brownian relaxation is directly proportional to the hydrodynamic volume.[4] At a given magnetic field and frequency, iron oxide nanoparticles between 12 and 20 nm typically yield the highest SAR values.[4,43,45] Smaller spherical iron oxide nanoparticles particles generally dissipate less heat.[43] Apart from size, particle magnetic properties (e.g., magnetic anisotropy and magnetization saturation), their colloidal stability, and size polydispersity play crucial roles, too.[4,27,43]

Finally, DLS analyses in complex media were performed and verified the effect of the PVA coating on particle colloidal stability (Figure S10). Particles coated with citric acid (20-CA) quickly aggregated, and partially flocculated, PVA-coated SPIONs (20-PVA) were stable in all experiments.

CONCLUSION

In summary, we demonstrate a method to design optimized SPIONs for magnetic hyperthermia by following a protocol employing a synthesis method with postprocessing. The synthesis that is used provides good control over particle size and low polydispersity. However, the particles that were coated with oleic acid, a surface ligand to stabilize them in organic solvents, and the larger SPIONs display inadequate crystallinity. To overcome these limitations, we demonstrate how a simple ligand exchange process can be used to simultaneously anneal the SPIONs and stabilize them in polar solvents. We observe that in the presence of oxygen the temperature of ligand exchange is the key parameter influencing the crystalline structure and the magnetic properties of the SPIONs. Furthermore, we correlate the heating power with respect to both size and crystallinity. SPIONs with 10 nm diameter do not produce detectable heat, and 20 nm SPIONs that have a wüstite core display poor hyperthermia properties. The purely magnetite SPIONs, on the other hand, have high heating power. Finally, we demonstrate that colloidal stability can be improved in biological media by coating the particles with polymer without affecting the SPIONs' behavior.

ASSOCIATED CONTENT

Supporting Information

The Supporting Information is available

Particles' characterization: TEM, DLS, ζ-potential, and iron quantification; crystalline structure analysis: high-resolution HAADF-STEM, EELS, and XRD; magnetic measurements: VSM and hyperthermia characterization and Mössbauer spectroscopy (PDF)

AUTHOR INFORMATION

Corresponding Author

*(A.F.) E-mail alke.fink@unifr.ch.

ORCID

Laura Rodriguez-Lorenzo: 0000-0002-0315-7981
Xiao Hua: 0000-0002-8673-5678
Sara Bals: 0000-0002-4249-8017
Sandor Balog: 0000-0002-4847-9845
Ann M. Hirt: 0000-0002-2193-0472
Marco Lattuada: 0000-0001-7058-9509
Alke Petri-Fink: 0000-0003-3952-7849

Author Contributions

F.C. designed the experiments, functionalized the particles, and performed TEM, DLS, XRD, VSM, and hyperthermia experiments. F.C. and L.H. synthesized the particles. F.C. and L.R.L. quantified the iron. X.H. analyzed the XRD data, B.G. and S.B.2 performed high-resolution TEM and EELS. J.S.G. performed Mössbauer spectroscopy, S.B.1 wrote the scripts for DLS, and D.B. synthesized the PVA-polymer. F.C., L.R.L., and A.P.F. wrote the manuscript with the contributions of X.H., S.B., A.M.H., J.S.G., B.R.R., and M.L. All authors have agreed on the manuscript.

Notes

The authors declare no competing financial interest.

ACKNOWLEDGMENTS

This work was supported by the Swiss National Science Foundation through the National Center of Competence in Research Bio-Inspired Materials, the Adolphe Merkle Foundation, the University of Fribourg, and the European Society for Molecular Imaging (Grant E141200643).

REFERENCES

(1) Gupta, A. K.; Gupta, M. Synthesis and Surface Engineering of Iron Oxide Nanoparticles for Biomedical Applications. *Biomaterials* **2005**, *26*, 3995−4021.

(2) Laurent, S.; Forge, D.; Port, M.; Roch, A.; Robic, C.; Vander Elst, L.; Muller, R. N. Magnetic Iron Oxide Nanoparticles: Synthesis,

Stabilization, Vectorization, Physicochemical Characterizations, and Biological Applications. *Chem. Rev.* **2008**, *108*, 2064−2110.
(3) Lee, N.; Yoo, D.; Ling, D.; Cho, M. H.; Hyeon, T.; Cheon, J. Iron Oxide Based Nanoparticles for Multimodal Imaging and Magnetoresponsive Therapy. *Chem. Rev.* **2015**, *115*, 10637−10689.
(4) Rosensweig, R. E. Heating Magnetic Fluid with Alternating Magnetic Field. *J. Magn. Magn. Mater.* **2002**, *252*, 370−374.
(5) Laurent, S.; Dutz, S.; Häfeli, U. O.; Mahmoudi, M. Magnetic Fluid Hyperthermia: Focus on Superparamagnetic Iron Oxide Nanoparticles. *Adv. Colloid Interface Sci.* **2011**, *166*, 8−23.
(6) Hergt, R.; Dutz, S.; Roder, M. Effects of Size Distribution on Hysteresis Losses of Magnetic Nanoparticles for Hyperthermia. *J. Phys.: Condens. Matter* **2008**, *20*, 385214.
(7) Vreeland, E. C.; Watt, J.; Schober, G. B.; Hance, B. G.; Austin, M. J.; Price, A. D.; Fellows, B. D.; Monson, T. C.; Hudak, N. S.; Maldonado-Camargo, L.; Bohorquez, A. C.; Rinaldi, C.; Huber, D. L. Enhanced Nanoparticle Size Control by Extending LaMer's Mechanism. *Chem. Mater.* **2015**, *27*, 6059−6066.
(8) Lak, A.; Kraken, M.; Ludwig, F.; Kornowski, A.; Eberbeck, D.; Sievers, S.; Litterst, F. J.; Weller, H.; Schilling, M. Size Dependent Structural and Magnetic Properties of FeO−Fe_3O_4 Nanoparticles. *Nanoscale* **2013**, *5*, 12286−12295.
(9) Estrader, M.; López-Ortega, A.; Golosovsky, I. V.; Estradé, S.; Roca, A. C.; Salazar-Alvarez, G.; López-Conesa, L.; Tobia, D.; Winkler, E.; Ardisson, J. D.; Macedo, W. A. A.; Morphis, A.; Vasilakaki, M.; Trohidou, K. N.; Gukasov, A.; Mirebeau, I.; Makarova, O. L.; Zysler, R. D.; Peiró, F.; Baró, M. D.; Bergström, L.; Nogués, J. Origin of the Large Dispersion of Magnetic Properties in Nanostructured Oxides: FexO/Fe 3O4 Nanoparticles as a Case Study. *Nanoscale* **2015**, *7*, 3002−3015.
(10) Sharma, S. K.; Vargas, J. M.; Pirota, K. R.; Kumar, S.; Lee, C. G.; Knobel, M. Synthesis and Ageing Effect in FeO Nanoparticles: Transformation to Core−shell FeO/Fe_3O_4 and Their Magnetic Characterization. *J. Alloys Compd.* **2011**, *509*, 6414−6417.
(11) Hai, H. T.; Yang, H. T.; Kura, H.; Hasegawa, D.; Ogata, Y.; Takahashi, M.; Ogawa, T. Size Control and Characterization of Wustite (core)/Spinel (shell) Nanocubes Obtained by Decomposition of Iron Oleate Complex. *J. Colloid Interface Sci.* **2010**, *346*, 37−42.
(12) Hou, Y.; Xu, Z.; Sun, S. Controlled Synthesis and Chemical Conversions of FeO Nanoparticles. *Angew. Chem., Int. Ed.* **2007**, *46*, 6329−6332.
(13) Chen, C. J.; Lai, H. I.; Lin, C. C.; Wang, J. S.; Chiang, R. K. Preparation of Monodisperse Iron Oxide Nanoparticles via the Synthesis and Decomposition of Iron Fatty Acid Complexes. *Nanoscale Res. Lett.* **2009**, *4*, 1343−1350.
(14) Bronstein, L. M.; Huang, X.; Retrum, J.; Schmucker, A.; Pink, M.; Stein, B. D.; Dragnea, B. Influence of Iron Oleate Complex Structure on Iron Oxide Nanoparticle. *Chem. Mater.* **2007**, *19*, 3624−3632.
(15) Park, J.; An, K.; Hwang, Y.; Park, J. G.; Noh, H. J.; Kim, J. Y.; Park, J. H.; Hwang, N. M.; Hyeon, T. Ultra-large-scale Syntheses of Monodisperse Nanocrystals. *Nat. Mater.* **2004**, *3*, 891−895.
(16) Sun, S.; Zeng, H. Size-controlled Synthesis of Magnetite Nanoparticles. *J. Am. Chem. Soc.* **2002**, *124*, 8204−8205.
(17) Sui, X.; Chen, Q.; Hempenius, M. A.; Vancso, G. J. Probing the Collapse Dynamics of Poly(N-isopropylacrylamide) Brushes by AFM: Effects of Co-nonsolvency and Grafting Densities. *Small* **2011**, *7*, 1440−1447.
(18) Hai, H. T.; Kura, H.; Takahashi, M.; Ogawa, T. Phase Transformation of Core/Shell Nanocubes and Facile Synthesis of Nanocubes. *J. Appl. Phys.* **2010**, *107*, No. 09E301.
(19) Redl, F. X.; Black, C. T.; Papaefthymiou, G. C.; Sandstrom, R. L.; Yin, M.; Zeng, H.; Murray, C. B.; O'Brien, S. P. Magnetic, Electronic, and Structural Characterization of Nonstoichiometric Iron Oxides at the Nanoscale. *J. Am. Chem. Soc.* **2004**, *126*, 14583−14599.
(20) Lak, A.; Niculaes, D.; Anyfantis, G. C.; Bertoni, G.; Barthel, M. J.; Marras, S.; Cassani, M.; Nitti, S.; Athanassiou, A.; Giannini, C.; Pellegrino, T. Facile Transformation of FeO/Fe_3O_4 Core-shell Nanocubes to Fe_3O_4 via Magnetic Stimulation. *Sci. Rep.* **2016**, *6*, 33295.
(21) Boni, A.; Albertazzi, L.; Innocenti, C.; Gemmi, M.; Bifone, A. Bifone A Water Dispersal and Functionalization of Hydrophobic Iron Oxide Nanoparticles with Lipid-modified Poly (amidoamine) Dendrimers. *Langmuir* **2013**, *29*, 10973−10979.
(22) Wang, L.; Luo, J.; Maye, M. M.; Fan, Q.; Rendeng, Q.; Engelhard, M. H.; Wang, C.; Lin, Y.; Zhong, C. J. Iron Oxide−gold Core−shell Nanoparticles and Thin Film Assembly. *J. Mater. Chem.* **2005**, *15*, 1821.
(23) Vogt, C.; Toprak, M. S.; Muhammed, M.; Laurent, S.; Bridot, J. L.; Müller, R. N. High Quality and Tuneable Silica Shell−magnetic Core Nanoparticles. *J. Nanopart. Res.* **2010**, *12*, 1137−1147.
(24) Lattuada, M.; Hatton, T. A. Functionalization of Monodisperse Magnetic Nanoparticles. *Langmuir* **2007**, *23*, 2158−2168.
(25) Burnand, D.; Monnier, C. A.; Redjem, A.; Schaefer, M.; Rothen-Rutishauser, B.; Kilbinger, A.; Petri-Fink, A. Catechol-derivatized Poly (vinyl alcohol) as a Coating Molecule for Magnetic Nanoclusters. *J. Magn. Magn. Mater.* **2015**, *380*, 157−162.
(26) Bossert, D.; Crippa, F.; Petri-Fink, A.; Balog, S. Hypothesis Test of the Photon Count Distribution for Dust Discrimination in Dynamic Light Scattering. *Anal. Chem.* **2018**, *90*, 3656−3660.
(27) Monnier, C. A.; Lattuada, M.; Burnand, D.; Crippa, F.; Martinez-Garcia, J. C.; Hirt, A. M.; Rothen-Rutishauser, B.; Bonmarin, M.; Petri-Fink, A. A lock-in-based Method to Examine the Thermal Signatures of Magnetic Nanoparticles in the Liquid, Solid and Aggregated States. *Nanoscale* **2016**, *8*, 13321−13332.
(28) Monnier, C. A.; Crippa, F.; Geers, C.; Knapp, E.; Rothen-Rutishauser, B.; Bonmarin, M.; Lattuada, M.; Petri-Fink, A. Lock-in Thermography as an Analytical Tool for Magnetic Nanoparticles: Measuring Heating Power and Magnetic Fields. *J. Phys. Chem. C* **2017**, *121*, 27164−27175.
(29) Le Caer, G.; Cadogan, J. M.; Brand, R. A.; Dubois, J. M.; Guntherodt, H. J. Sign Determination of the 57Fe Quadrupole Splitting in an Amorphous Fe24Zr76 alloy. *J. Phys. F: Met. Phys.* **1984**, *14*, L73−L78.
(30) Fischer, R. A.; Campbell, A. J.; Lord, O. T.; Shofner, G. A.; Dera, P.; Prakapenka, V. B. Phase Transition and Metallization of FeO at High Pressures and Temperatures. *Geophys. Res. Lett.* **2011**, *38*, 2−6.
(31) Řezníček, R.; Chlan, V.; Štěpánková, H.; Novák, P.; Zukrowski, J.; Kozłowski, A.; Kakol, K.; Tarnawski, Z.; Honig, J. M. Understanding the Mössbauer Spectrum of Magnetite Below the Verwey Transition: Ab Initio Calculations, Simulation, and Experiment. *Phys. Rev. B: Condens. Matter Mater. Phys.* **2017**, *96*, 195124.
(32) Gheisari, M.; Mozafari, M.; Niyaifar, M.; Amighian, J.; Soleimani, R. Observation of Small Exchange Bias in Defect Wüstite (Fe0.93O) Nanoparticles. *J. Supercond. Novel Magn.* **2013**, *26*, 237−242.
(33) Dimitrov, D. V.; Unruh, K.; Hadjipanayis, G. C.; Papaefthymiou, V.; Simopoulos, A. Ferrimagnetism and Defect Clusters in $Fe_{1-x}O$ films. *Phys. Rev. B: Condens. Matter Mater. Phys.* **1999**, *59*, 499−504.
(34) Cornell, R. M.; Schwertmann, U. *The Iron Oxides*; WCH GmbH: Weinheim, Germany, 1996.
(35) Bonnaud, C.; Monnier, C. A.; Demurtas, D.; Jud, C.; Vanhecke, D.; Montet, X.; Hovius, R.; Lattuada, M.; Rothen-Rutishauser, B.; Petri-Fink, A. Insertion of Nanoparticle Clusters into Vesicle Bilayers. *ACS Nano* **2014**, *8*, 3451−3460.
(36) Monego, D.; Kister, T.; Kirkwood, N.; Mulvaney, P.; Widmer-Cooper, A.; Kraus, T. Colloidal Stability of Apolar Nanoparticles: Role of Ligand Length. *Langmuir* **2018**, *34*, 12982−12989.
(37) Hufschmid, R.; Arami, H.; Ferguson, R. M.; Gonzales, M.; Teeman, E.; Brush, L. N.; Browning, N. D.; Krishnan, K. M. Synthesis of Phase-pure and Monodisperse Iron Oxide Nanoparticles by Thermal Decomposition. *Nanoscale* **2015**, *7*, 11142−11154.
(38) Berkowitz, A. E.; Kodama, R. H.; Makhlouf, S. A.; Parker, F. T.; Spada, F. E.; McNiff, E. J.; Foner, S. Anomalous Properties of

Magnetic Nanoparticles. *J. Magn. Magn. Mater.* **1999**, *196–197*, 591–594.
(39) Kodama, R. H.; Berkowitz, A. E. Atomic-scale Magnetic Modeling of Oxide Nanoparticles. *Phys. Rev. B: Condens. Matter Mater. Phys.* **1999**, *59*, 6321–6336.
(40) Morales, P. M.; Veintemillas-Verdaguer, S.; Montero, M. I.; Serna, C. J.; Roig, A.; Casas, L.; Martínez, B.; Sandiumenge, F. Surface and Internal Spin Canting in γ-Fe_2O_3 Nanoparticles. *Chem. Mater.* **1999**, *11*, 3058–3064.
(41) Leszczyński, B.; Hadjipanayis, G. C.; El-Gendy, A. A.; Załęski, K.; Śniadecki, Z.; Musiał, A.; Jarek, M.; Jurga, S.; Skumiel, A. The Influence of Oxidation Process on Exchange Bias in Egg-Shaped FeO/Fe_3O_4 Core/Shell Nanoparticles. *J. Magn. Magn. Mater.* **2016**, *416*, 269–274.
(42) Kallumadil, M.; Tada, M.; Nakagawa, T.; Abe, M.; Southern, P.; Pankhurst, Q. A. Suitability of Commercial Colloids for Magnetic Hyperthermia. *J. Magn. Magn. Mater.* **2009**, *321*, 1509–1513.
(43) Deatsch, A. E.; Evans, B. A. Heating Efficiency in Magnetic Nanoparticles Hyperthermia. *J. Magn. Magn. Mater.* **2014**, *354*, 163–172.
(44) Cheraghipour, E.; Javadpour, S.; Mehdizadeh, A. R. Citrate Capped Superparamagnetic Iron Oxide Nanoparticles Used for Hyperthermia Therapy. *J. Biomed. Sci. Eng.* **2012**, *5*, 715–719.
(45) Fortin, J. P.; Wilhelm, C.; Servais, J.; Ménager, C.; Bacri, J. C.; Gazeau, F. Size-Sorted Anionic Iron Oxide Nanomagnets as Colloidal Mediators for Magnetic Hyperthermia. *J. Am. Chem. Soc.* **2007**, *129* (9), 2628–2635.